Journal of Materials Chemistry A

COMMUNICATION

View Article Online
View Journal | View Issue

Cite this: J. Mater. Chem. A, 2016, 4, 8554

Received 15th April 2016
Accepted 10th May 2016

DOI: 10.1039/c6ta03115c

www.rsc.org/MaterialsA

Film-through large perovskite grains formation *via* a combination of sequential thermal and solvent treatment†

Fan Zhang,‡[abc] Jun Song,‡[ab] Linxing Zhang,[ab] Fangfang Niu,[ab] Yuying Hao,[c] Pengju Zeng,[ab] Hanben Niu,*[abc] Jinsong Huang[d] and Jiarong Lian‡*[ab]

Organic–inorganic halide perovskites have recently attracted strong research interest for fabrication of high-performance, low-cost photovoltaic devices. Recently, we reported a highly reproducible procedure to fabricate high-performance organic–inorganic halide perovskite solar cells. This procedure, based on a one-step, solvent-induced, fast deposition-crystallization method, involves the use of *sec*-butyl alcohol as a new solvent to induce the $CH_3NH_3PbI_3$ fast crystallization deposition. In the present study, we propose a reproducible fabrication method to prepare both flat and large-grain perovskite film by adding a pre-annealing step to strengthen the perovskite nucleation, aiming to facilitate the excess CH_3NH_3I and solvent removal in the *sec*-butyl alcohol soaking process, in which all films with thickness between 420 nm and 1 μm performed uniformly. The best performing planar device obtained with this procedure had an efficiency of 17.2% under AM 1.5G illumination and an average power conversion efficiency of 16.2 ± 0.5%. We also analyzed the efficiency of halide perovskite planar solar cells as a function of the perovskite film thickness; the efficiency dropped only slightly to 15.7% when the perovskite film thickness was increased to 1 μm.

Introduction

Organic–inorganic halide perovskites have recently attracted strong research interest owing to their excellent optical, electronic, and material properties such as high absorption coefficient, high open-circuit voltage (V_{OC}) from small exciton binding energy, long charge carrier diffusion length by formation of shallow traps, and low temperature solution processibility.[1–8] Since the first report of perovskite materials in photovoltaic devices, published in 2009, organometallic lead-halide perovskite solar cells have shown one of the most rapid growths ever in photovoltaic history.[9–13] Within a short period of time, the certified power conversion efficiency (PCE) of perovskite solar cells has already exceeded 21%.[14] These results suggest an enormous potential for perovskite compounds as efficient photoactive materials for photovoltaic applications.[15–18]

Lead-halide perovskite films can be deposited on substrates through *in situ* reactions of precursors *via* single- or two-step methods.[19,20] Two types of device architectures are typically adopted in perovskite solar cells. It was initially assumed that a mesostructured (or nanostructured) matrix may be necessary for efficient charge transport and collection in perovskite solar cells.[21] To simplify the device architecture and processing procedures, planar architectures without mesoporous layers were proposed and proved to be very suitable for perovskite solar cells, owing to long charge diffusion lengths.[22,23] To avoid shunting in such planar devices, a nonporous homogenous perovskite film must be deposited. However, films produced by the conventional spin-coating methods were found to be composed of large $CH_3NH_3PbI_3$ grains and many uncovered pin-hole areas.[24] Therefore, to achieve optimum film morphology, effective ways to manipulate nucleation and growth of perovskite crystals in solution-processed systems, particularly in planar systems, are highly sought after.

Recently, a new method called "solvent engineering" was proposed in one-step spin coating to fabricate perovskite layers with uniform and dense planar geometry. Jeon *et al.* reported that the perovskite film was deposited from a precursor solution dissolved in a mixture of dimethyl sulfoxide (DMSO) and γ-butyrolactone (GBL) (DSMO : GBL = 3 : 7 v/v), immediately followed by a toluene drip while the substrate was spinning.[25] Independently, Xiao *et al.* reported that flat and uniform perovskite thin films can be obtained by a fast deposition-

[a]Institute of Optoelectronics, Key Lab of Optoelectronics Devices, Systems of Ministry of Education/Guangdong Province, Shenzhen University, 518060, Shenzhen, China. E-mail: ljr@szu.edu.cn; niuhb@szu.edu.cn

[b]Key Laboratory of Micro-Nano Measuring and Imaging in Biomedical Optics, College of Optoelectronic Engineering, Shenzhen University, Shenzhen 518060, China

[c]Key Laboratory of Advanced Transducers and Intelligent Control System (Ministry of Education), Taiyuan University of Technology, Taiyuan 030024, China

[d]Department of Mechanical and Materials Engineering, Nebraska Center for Materials and Nanoscience, University of Nebraska-Lincoln, Lincoln, Nebraska 68588-0656, USA

† Electronic supplementary information (ESI) available. See DOI: 10.1039/c6ta03115c

‡ These authors contributed equally to this work.

crystallization (FDC) method involving spin coating from a dimethyl formamide (DMF) solution, followed by chlorobenzene (CB) dripping during the spin coating to induce crystallization.[26] This approach greatly resembles the solvent engineering method (DMSO/GBL/toluene) developed by Jeon *et al.* Despite the similarity in protocols, the results are very different. The presence of DMSO, which strongly coordinates with lead halides by forming intermediate phases, prevents immediate crystallization upon toluene drip, as observed from the lack of color change in the film. On the other hand, the CB drip instantly promotes darkening, which suggests instantaneous perovskite formation. These methods, based on the use of toluene or chlorobenzene, are not applicable to massive production, owing to their high toxicity and cost. Recently, we verified the validity of this process by using *sec*-butyl alcohol as a new solvent, both in the washing step to promote fast crystallization and in the soaking step, to remove excessive methylammonium iodide (MAI) content in $CH_3NH_3PbI_3$ films.[27] Although good PCEs of approximately 14.3% were achieved, they were limited by the poor quality of perovskite film when its thickness was increased.

Herein, we report an improved fabrication procedure which is applicable to fabricate perovskite films with larger thickness and superior crystal morphology. In this procedure, a thermal pre-annealing proved to be a crucial step in improving the growth of perovskite film morphology. The best-performing planar structure device, obtained with pre-annealing at 100 °C, exhibited an efficiency of 17.2% under AM 1.5G illumination and an average PCE of 16.2 ± 0.5% over 40 cells. We also examined the efficiency of halide perovskite planar-structure solar cells as a function of the thickness variation of the perovskite films, finding that the efficiency dropped only slightly to 15.7% when the perovskite film thickness was increased to about 1 μm.

Results and discussion

Fig. 1 shows a schematic representation of the adopted fabrication process. The perovskite precursor solution was prepared by mixing 922 mg PbI_2 (99.999%, Alfa Aesar) and 349.8 mg CH_3NH_3I in 0.9 mL of DMF (99.5%, Sigma-Aldrich) and 0.1 mL of DMSO (99.5%, Sigma-Aldrich), with PbI_2 : CH_3NH_3I molar ratio of 1 : 1.1. The mixture solution was spin coated on the poly(3,4-ethylenedioxythiophene)–polystyrene sulfonate (PEDOT:PSS) layer at 6000 rpm and, after 7–9 seconds of delay time depending on the concentration of the precursor solution, the wet film was washed with *sec*-butyl alcohol (99.5%, Sigma-Aldrich) (washing step). After *sec*-butyl alcohol was uniformly dropped in the center of the substrate, the perovskite film quickly changed to a dark brown color. The *sec*-butyl alcohol rapidly reduced the solubility of perovskite in the mixed solvent, promoting fast nucleation and crystal growth. After the spinning stopped, the film was annealed on a hot plate at 100 °C for ~30 s (defined as the pre-annealing step), quickly showing a black color with a mirror-like surface. The film was then soaked with *sec*-butyl alcohol for a few seconds to remove excess MAI by accurately controlling the soaking time. Subsequently, the film was dried by spinning the substrates at 6000 rpm for 30 s and subjected to post-annealing treatment (post-annealing step). In this step, the perovskite film was transferred to the air condition in a super clean room with a controlled humidity of 55–65% for the post annealing process, which involves initial thermal annealing at 100 °C for 15 min and consequential solvent annealing in DMF atmosphere at 100 °C for 15 min. More descriptions of the experimental process can be found in the ESI.†

In this procedure, every step was carefully optimized to benefit the film fabrication. Excessive MAI (PbI_2 : MAI = 1 : 1.1 molar ratio) was purposed to supplement the consumption of MAI during the *sec*-butyl alcohol washing and soaking steps. This is because *sec*-butyl alcohol washing and soaking steps can remove a considerable quantity of MAI. The *sec*-butyl alcohol washing and soaking steps in this process promoted formation of the crystalline perovskite film, as in our previously reported approach,[27] in which *sec*-butyl alcohol was used to induce the $CH_3NH_3PbI_3$ fast crystallization and obtain an appropriate MAI content in $CH_3NH_3PbI_3$ films. It is thought that the solvent vapor in post annealing process plays a key role in determining the morphology and crystallinity of perovskite film, of which an improved perovskite film can be obtained by using either of the controlled moisture[32,33] and DMF atmosphere.[28,29] Thus, we optimized the post-annealing process by using initial thermal annealing in air and consequential solvent annealing in a DMF atmosphere. The pre-annealing step, which was added to our previously adopted procedure, played an important role in promoting the growth of perovskite grains.

The morphology dependence of the final perovskite films on the pre-annealing treatment was investigated by SEM. All films were prepared on ITO/PEDOT:PSS substrates to ensure identical conditions for the working device. Four representative samples obtained at different pre-annealing temperatures (w/o, 80, 100, and 120 °C) were analyzed, and their SEM images are shown in Fig. 2. The top-view SEM image of the $CH_3NH_3PbI_3$ perovskite film prepared without pre-annealing step (Fig. 2a) shows a surface with fine and irregular crystallites, and the grain size was estimated to be 560 nm on average as shown in Fig. S1 of ESI.† However, some voids are found at the bottom (close to the PEDOT:PSS layer) of the film from the cross-sectional SEM

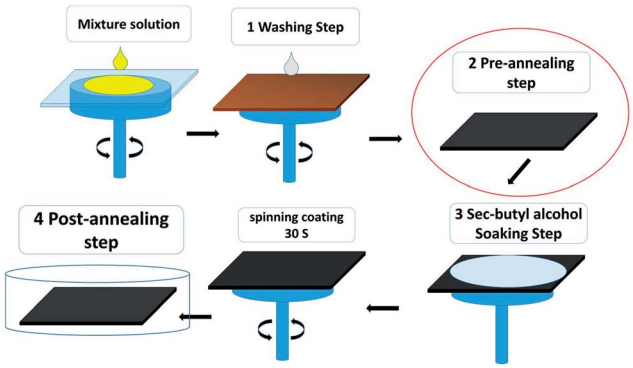

Fig. 1 Schematic illustration of the fabrication procedure including washing, pre-annealing, soaking, and post-annealing steps.

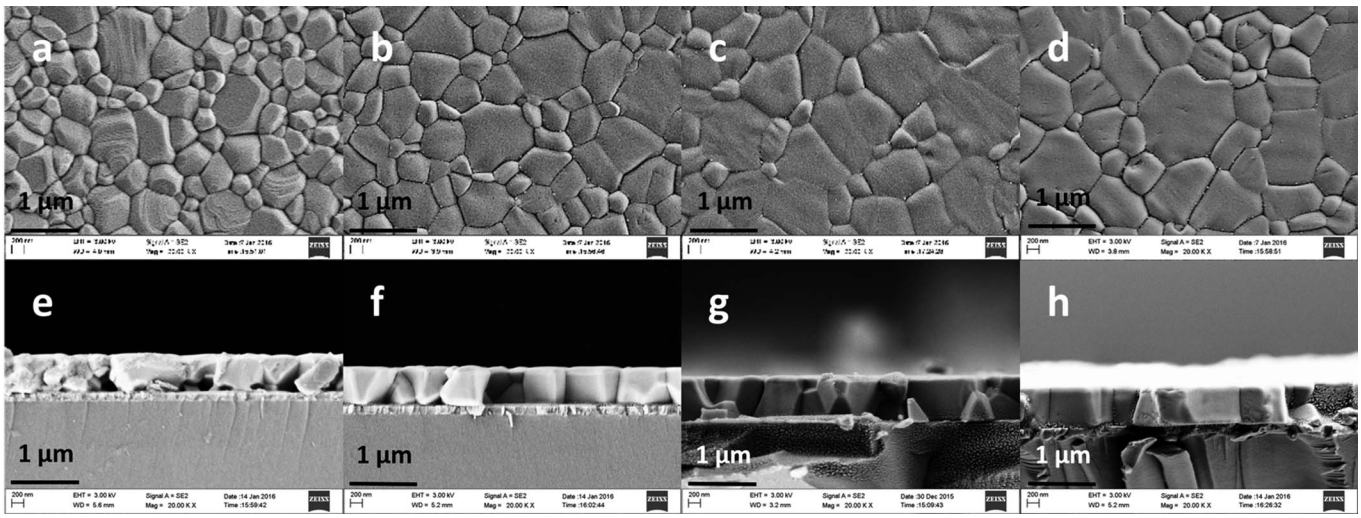

Fig. 2 Top-view (a–d) and cross-sectional (e–h) scanning electron microscopy image of $CH_3NH_3PbI_3$ perovskite films prepared using different pre-annealing temperatures: (a and e) without pre-annealing step, (b and f) 80 °C, (c and g) 100 °C, and (d and h) 120 °C.

image of the same film in Fig. 2e. When a pre-annealing temperature at 80 °C was used, the final perovskite film surface exhibited more uniform morphology and larger crystal grain size with an average grain size of 731.5 nm (Fig. 2b). The voids are also greatly reduced and even disappeared (Fig. 2f–h). The grain size of the perovskite films are even larger when we continued increasing the pre-annealing temperature up to 100 °C and 120 °C, and then more than 80% of the given area was occupied by 1–2 μm large grains. It should be noted that all the films using the pre-annealing step show film-through large gain distribution, which is the ideal condition for high performance PSCs because the charges could be transported and collected through a single grain without encountering grain boundaries and charge traps.

Photoluminescence (PL) spectra were measured to verify the composition and structure evolution of the perovskite film. An excitation light of 325 nm came into the films from the air side, and the PL signal was also collected from the air side. As shown in Fig. 3a, the PL spectra of perovskite film with 100 °C-pre-annealing exhibit a PL peak at 788 nm, which is blue-shifted relative to the film without pre-annealing (794 nm). Generally, the PL emission is related to the recombination channel concerning the bandgap and trap state. The blue-shift phenomenon may imply the film with 100 °C-pre-annealing has lower trap density around the band-edge than the film without. UV-Vis absorption spectra of the films with and without pre-annealing (100 °C) are compared in Fig. 3b. Note that the baselines for the UV-vis spectra without pre-annealing at long wavelengths are very high, because of the high light scattering associated with a rough perovskite film. Compared with that of the sample without pre-annealing treatment, the absorption of the film pre-annealed at 100 °C is stronger at wavelengths in the range of 400–600 nm. The neat perovskite composition for both films of w/o and with pre-annealing treatment can be deduced by showing sole $CH_3NH_3PbI_3$ diffraction peaks in Fig. 3c, and a slightly increased (110) orientation can also be obtained by using pre-annealing treatment.

On the basis of detailed investigation of the growth of perovskite films, a crystal growth model shown in Fig. 4 was proposed. *sec*-Butyl alcohol rapidly reduces the solubility of $CH_3NH_3PbI_3$ in the mixed solvent, thereby promoting fast nucleation and crystal growth on top of the perovskite film. However, when the perovskite film is thick enough (>600 nm), the solvent and some excessive MAI may remain at the bottom

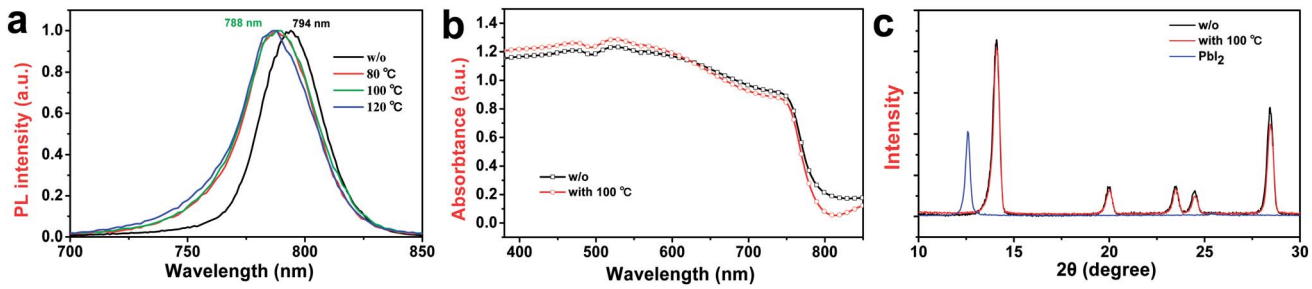

Fig. 3 (a) Normalized photoluminescence spectra (PL) of perovskite thin films prepared with different pre-annealing temperature. An excitation light of 325 nm irradiated on the film from the air side, and the PL signal was also collected from the air side. (b) Absorption spectra and (c) X-ray diffraction patterns of $CH_3NH_3PbI_3$ perovskite films prepared with and without pre-annealing step. The $CH_3NH_3PbI_3$ films were spun on the surface of an ITO/PEDOT:PSS layer to ensure the identical condition to the working device.

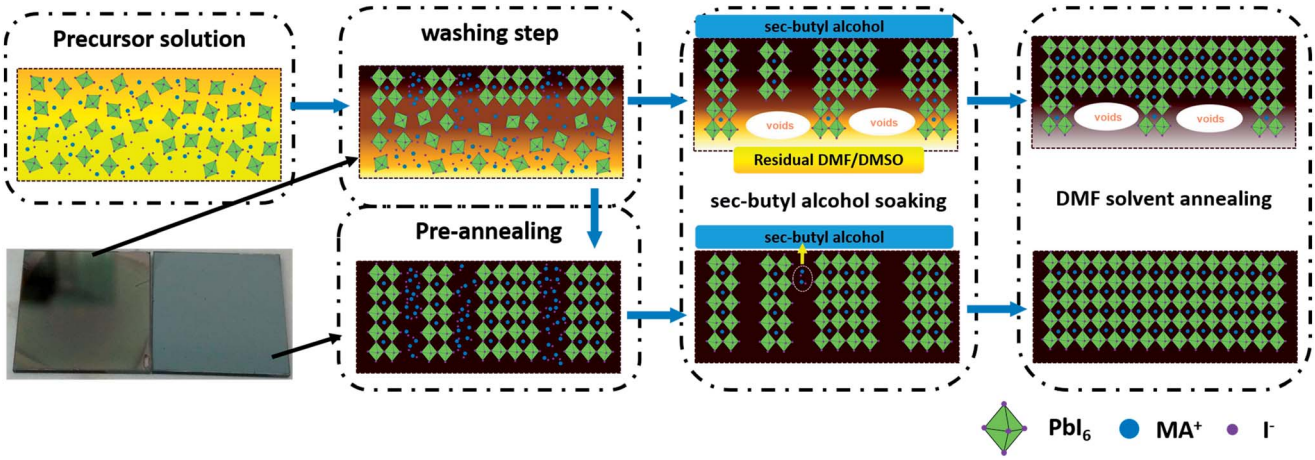

Fig. 4 Schematic illustration of the perovskite crystal growing process, including washing, pre-annealing, soaking, and post-annealing steps.

of the film. It is speculated that perovskite precursors are generally colloidal dispersions in this residual solvent with a colloidal size up to the mesoscale, rather than real solutions.[30] The colloid is made of a soft coordination complex in the form of a lead polyhalide framework between organic and inorganic components. In the case of film w/o pre-annealing treatment, the solvent and excessive MAI underneath are more difficult to be extracted out due to their coordination in colloid structure and the limited quantity penetration of *sec*-butyl alcohol, therefore an undesired film morphology with voids and small grains was formed after these solvent and excessive MAI were removed in the post annealing process. Here the existence of many defects can be reflected by longer wavelength location for the PL peaks as shown in Fig. 3a. When the thermal pre-annealing treatment is in use, these coordination would be interrupted due to the structure transformation from colloid to perovskite, so an enhanced *sec*-butyl alcohol penetration is obtained and large quantities of residual solvent and excessive MAI are extracted out in the *sec*-butyl alcohol soaking process. Finally, the perovskite crystals and morphology grow more extensively because of employing DMF solvent annealing. Both PbI_2 and CH_3NH_3I precursors are highly soluble in DMF vapor, and so can facilitate the diffusion and reorganization of the precursor molecules and ions.[28,29]

To probe the effect of the pre-annealing treatment on the photovoltaic performance, perovskite solar cells with a device structure of ITO/PEDOT:PSS/$CH_3NH_3PbI_3$/PCBM/Bphen/Al (Fig. 5) were fabricated for comparison. Here a 4,7-diphenyl-1,10-phenanthroline (Bphen) interfacial layer with a concentration of 0.7 mg mL^{-1} in ethanol was used to facilitate electron collection and to block aluminum penetration.[31] Photovoltaic metrics of the PSCs using pre-annealed treatment at different temperatures are summarized in Fig. 6a–d. Fig. 6e shows the typical *J*–*V* curves for each device, and their average photovoltaic performances are also listed in Table S2.† The reference devices without the pre-annealing step exhibited low performances with a PCE of 12.4 ± 1.1%, V_{OC} of 0.871 ± 0.035 V, short-circuit current density (J_{SC}) of 20.47 ± 1.50 mA cm^{-2}, and FF of 0.704 ± 0.021, respectively. While pre-annealing treatment is in use, all the PSCs show significantly enhanced photovoltaic performances. Taking the devices with pre-annealing temperature at 100 °C for an example, their PCE, V_{OC}, J_{SC}, and FF were increased to 16.6 ± 0.5%, 0.972 ± 0.008 V, 22.25 ± 0.32 mA cm^{-2}, and 0.766 ± 0.007, respectively.

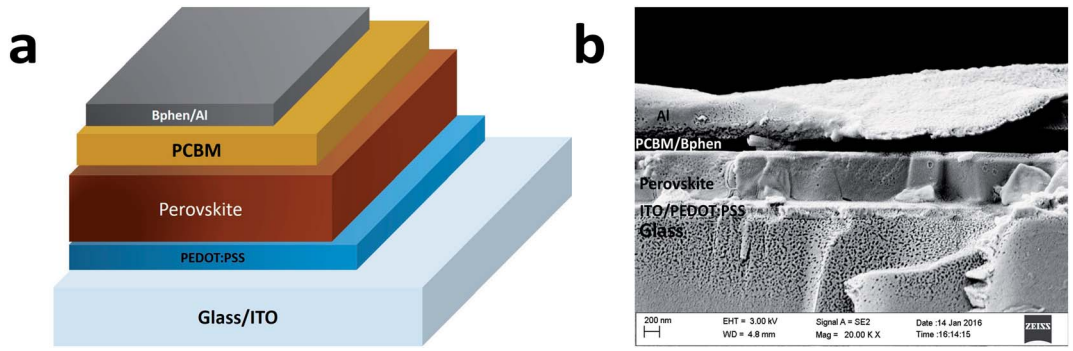

Fig. 5 (a) Schematic device structure of a perovskite solar cell; the devices were structured as ITO/PEDOT:PSS/$CH_3NH_3PbI_3$/PCBM/Bphen/Al. (b) Cross-sectional scanning electron microscopy image of the full perovskite solar cell under 100 °C pre-annealing conditions.

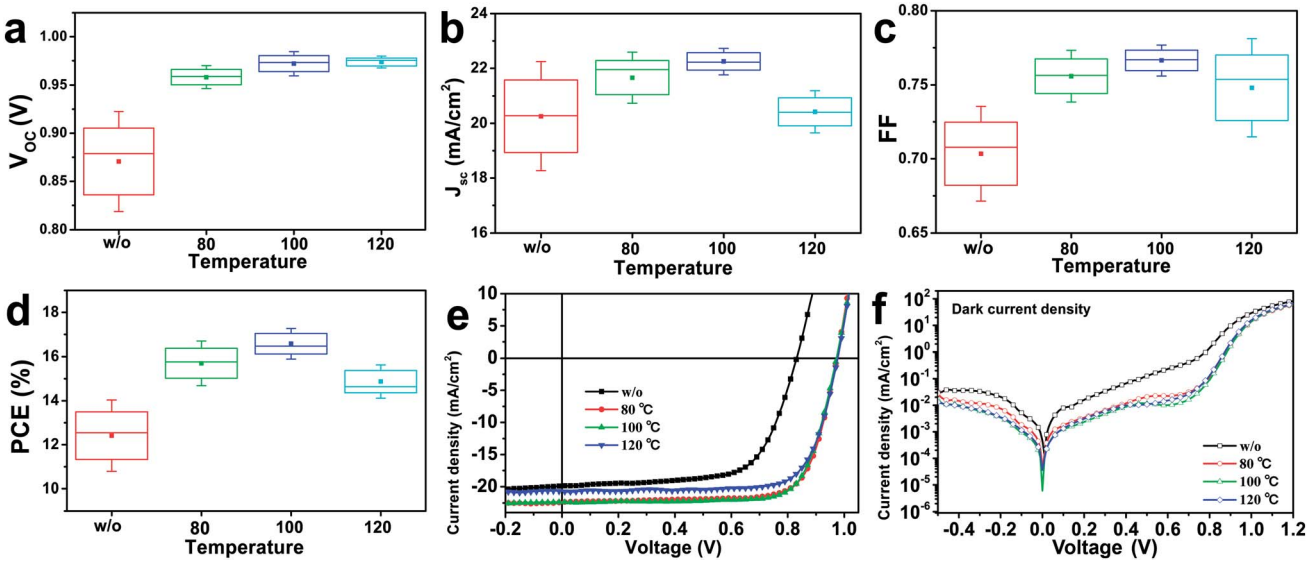

Fig. 6 Influence of pre-annealing step on the fabricated solar cells. Short-circuit current density (J_{SC}) (a) open-circuit voltage (V_{OC}), (b) fill factor (FF), (c) power conversion efficiency (PCE), and (d) of perovskite solar cell devices prepared at different pre-annealing temperatures of 6 cells. *J–V* curves of devices with different pre-annealing temperatures: (e) the *J–V* data were collected under AM 1.5G one sun illumination (100 mW cm^{-2}), (f) the *J–V* data were collected under dark.

Here the increased J_{SC} can be explained by more effective carrier collection, because the ideal perovskite morphology with film-through large grains (seen in Fig. 2) makes carriers transport and be collected through a single grain without encountering grain boundaries and charge traps. To find the origin of the enhanced V_{OC}, we compared their dark current curves of all devices, because V_{OC} for the given photoactive materials is determined by the equation:

$$V_{OC} = \frac{nK_BT}{q} \ln\left(\frac{J_{SC}}{J_o}\right) \quad (1)$$

where n, K_B, T, q, J_{SC}, and J_o stand for ideal factor, Boltzmann constant, absolute temperature, electron charge, short current density, and saturated reversed current density, respectively.

According to the expression of the dark current density (J_D):

$$J_D = J_o\left(e^{\frac{qV}{nK_BT}} - 1\right) \quad (2)$$

As shown in Fig. 6f, it is easy to know that the dark current of the device was decreased about one order of magnitude when pre-annealing is in use, so then lower J_o can be expected. Therefore, the obvious increased V_{OC} can be interpreted by the combination of larger J_{SC} and lower J_o.

Here the photocurrent hysteresis characteristics for all devices have also been studied as shown in Fig. S2.† It is clear that the pre-annealing treatment is very effective in suppressing the undesired hysteresis phenomenon of a device. For the conventional device, obvious changes from 11.0% to 12.5% in PCE, and from 0.83 V to 0.88 V in V_{OC}, are found when the voltage scan direction was changed from forward to a reversed one. In contrast, we measured a 100 °C-pre-annealing device by changing the scanning directions (Fig. S2c†) and scanning rates (Fig. S3†) and this photocurrent hysteresis disappeared. This is consistent with previous studies reporting that charge traps are one of the origins of photocurrent hysteresis and, consequently, hysteresis can be reduced when the numerous voids and lots of crystal boundaries due to small grain size that are the principle source for traps, are excluded.

In addition, aiming to clarify why the device showed a reduced photovoltaic performance, while their perovskite films exhibited similar morphology (seen in Fig. 2) and the same profile in PL spectra (seen in Fig. 3a), we tried to study the role of defects in the film. As we know, the temperature for perovskite nucleation and crystal growth is no more than 100 °C which is the typical thermal annealing temperature as reported,[25,26] so a higher temperature thermal annealing may increase the formation possibility of crystal defects. Although similar profile were found in both PL spectra and morphology of perovskite films when the pre-annealing temperature was increased from 100 °C to 120 °C, a slight reduction of about 25% in PL intensity could be found (as shown in Fig. S4†), which was indicated by the increased traps and defects.

Fig. 7a shows the *J–V* curve of the best performing device obtained under 100 °C pre-annealing conditions, which exhibited a J_{SC} of 22.6 mA cm^{-2}, a FF of 77.3%, a V_{OC} of 0.98 V, and a PCE of 17.2%. The external quantum efficiency (EQE) of the same device is shown in Fig. 5b. The EQE value was higher than 80% over the whole visible region, reaching a maximum value of about 90%. The calculated J_{SC} from the EQE spectra is 21.83 mA cm^{-2}, which is comparable to our experimental value. To confirm the high reproducibility and slight efficiency deviation, the statistics of FF, J_{SC}, V_{OC}, and PCE based on 40 devices are shown in Fig. 7c. Here the photovoltaic performance deviation is 22.03 ± 0.57 mA cm^{-2} for J_{SC}, is 0.759 ± 0.011 for FF, is

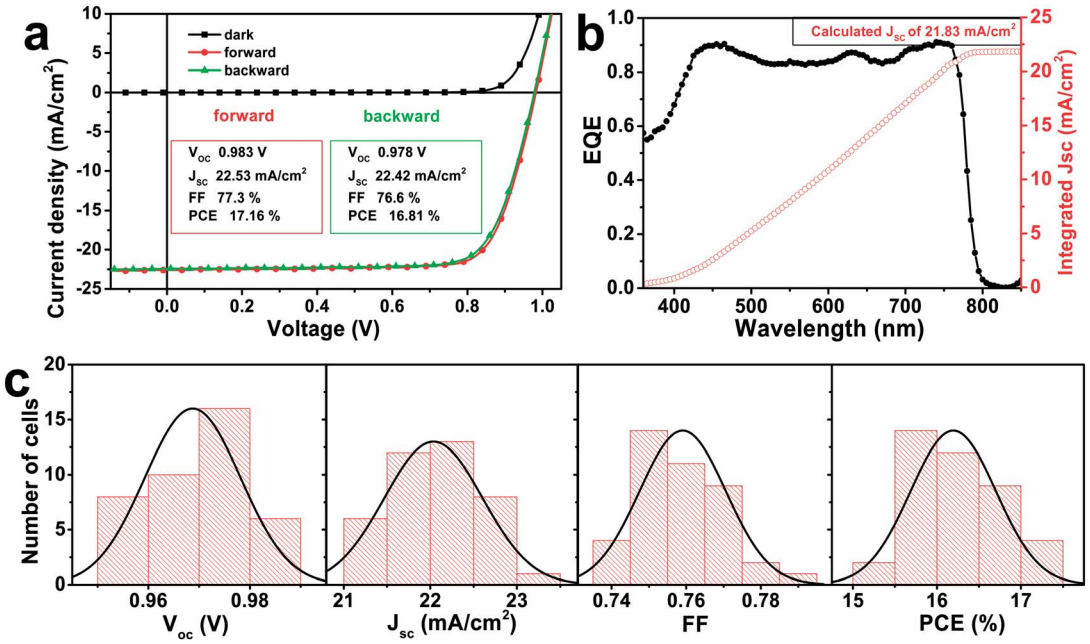

Fig. 7 (a) J–V curves and (b) external quantum efficiency (EQE) spectrum together with EQE data based integrated short-circuit current density (J_{SC}) for the best performing perovskite solar cell. The J–V data were collected under AM 1.5G one sun illumination (100 mW cm^{-2}). (c) Histograms of J_{SC}, open-circuit voltage (V_{OC}), fill factor (FF), and power conversion efficiency (PCE) of 40 cells, respectively.

0.969 ± 0.009 V for V_{OC}, and is 16.19 ± 0.51% for PCE, respectively.

Notably, the grains of the perovskite films reached in-plane sizes up to 1–2 μm, which was between two and three times the grain size along the thickness direction of the film (~650 nm). Such a high aspect ratio growth of the perovskite grains and low trap density in these films indicated that the adopted fabrication process allow producing thicker perovskite films. We analyzed the performance of halide perovskite planar solar cells as a function of the perovskite film thickness variation. To control the thickness of the perovskite film, we adjusted the concentrations of different solutions, obtaining thickness values from 420 to 1020 nm. The fabrication parameters for different thickness values are summarized in Table S1.† Top-view and cross-sectional SEM images of perovskite films with different thickness are shown in Fig. 8. All films with thickness from 420 nm to 1 μm performed uniformly and produced film-through grains. The photovoltaic parameters of the device with perovskite thickness from 420 nm to 1020 nm are listed in Table 1, and their photocurrent curves are shown in Fig. S5a.† The devices did not exhibit a strong dependency of device performance on film thickness, of which even the thickest device

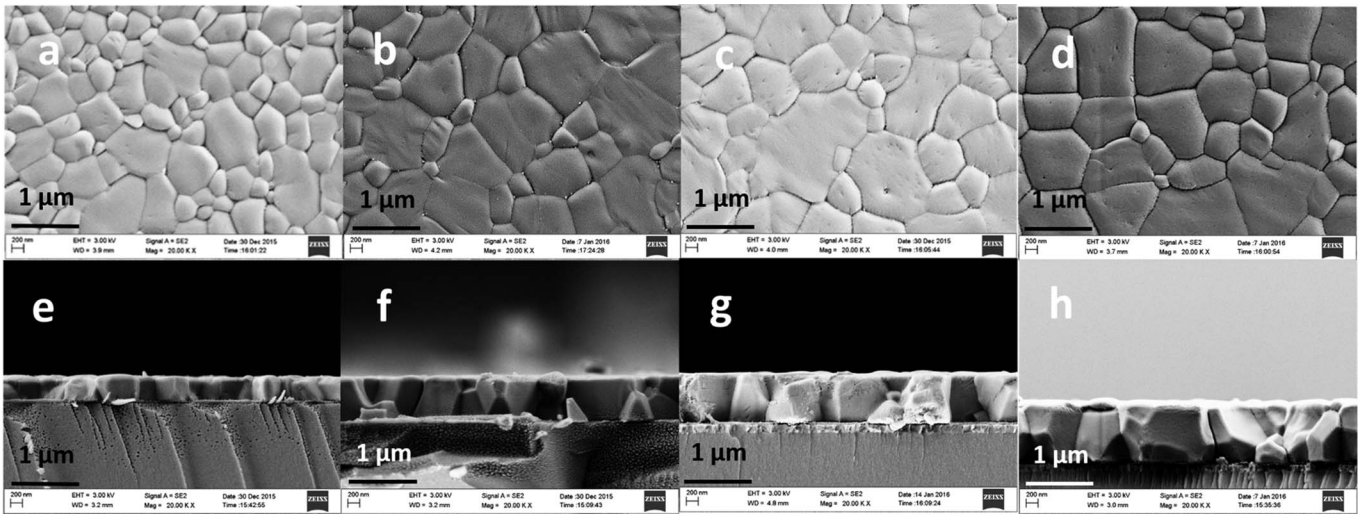

Fig. 8 Top-view (a–d) and cross-sectional (e–h) SEM image of $CH_3NH_3PbI_3$ perovskite films prepared with different thickness: (a and e) ~420 nm, (b and f) ~650 nm, (c and g) ~850 nm, and (d and h) ~1020 nm.

Table 1 Photovoltaic performance of perovskite solar cells with different thickness

Thickness (nm)	V_{OC} (V)	J_{SC} (mA cm^{-2})	FF	PCE (%)
~420	0.969	−21.45	71.1	14.77
~650	0.969	−21.97	76.2	16.23
~850	0.983	−20.73	75.1	15.31
~1020	0.983	−21.13	75.6	15.71

(1 μm film) still yielded PCE approaching 15.7%. The EQE spectra of the devices are shown in Fig. S5b;† all the devices show the comparable EQE characteristics, and the calculated J_{SC} even for 1020 nm-thick device is 21.14 mA cm^{-2}, which suggests that negligible photogenerated charge loss happens in a thick perovskite film because the charges could transport through a single grain without encountering grain boundaries and charge traps before being collected by the electrodes.

Conclusion

In summary, we developed an effective procedure to produce $CH_3NH_3PbI_3$ perovskite films with excellent crystallinity and large film-through grains. The pre-annealing step played an important role in promoting the growth of perovskite morphology and crystal behavior, resulting in a significant improvement of the material and electronic properties as well as a performance enhancement of the photovoltaic devices. The application of this procedure to solar cell fabrication yielded the highest PCE of 17.2% under AM 1.5G, 100 mW cm^{-2} test conditions. The devices did not exhibit a strong dependency of device performance on film thickness; even the thickest perovskite film prepared (1 μm thick) was able to yield PCE approaching 15.7%. Based on our results, we believe that this *sec*-butyl alcohol based procedure may provide a cleaner and more effective strategy for the realization of high-performance perovskite solar cells.

Acknowledgements

Parts of this work were supported by the National Basic Research Program of China (Grant No. 2015CB352005); the National Natural Science Foundation of China (No. 61525503/61378091/61405123/61505123); Guangdong Natural Science Foundation (No. S2012020011003 and 2014A030312008); Shenzhen Basic Research Project (JCYJ20130329115524512/ZDSYS20140430164957663/KQCX20140509172719305/JCYJ20150525092940976); the Training Plan of Guangdong Province Outstanding Young Teachers in Higher Education Institutions (Yq2013142).

Notes and references

1 H. Zhou, Q. Chen, G. Li, S. Luo, T. B. Song, H. S. Duan, Z. Hong, J. You, Y. Liu and Y. Yang, *Science*, 2014, **345**, 542.
2 J. Burschka, N. Pellet, S.-J. Moon, R. Humphry-Baker, P. Gao, M. K. Nazeeruddin and M. Grätzel, *Nature*, 2013, **499**, 316.
3 W. A. Laban and L. Etgar, *Energy Environ. Sci.*, 2013, **6**, 3249–3253.
4 H. Kim, K. G. Lim and T. W. Lee, *Energy Environ. Sci.*, 2016, **9**, 12–30.
5 M. M. Lee, J. Teuscher, T. Miyasaka, T. N. Murakami and H. J. Snaith, *Science*, 2012, **338**, 643.
6 G. Xing, N. Mathews, S. Sun, S. S. Lim, Y. M. Lam, M. Grätzel, S. Mhaisalkar and T. C. Sum, *Science*, 2013, **342**, 344.
7 C. S. Ponseca Jr, T. J. Savenije, M. Abdellah, K. Zheng, A. Yartsev, T. Pascher, T. Harlang, P. Chabera, T. Pullerits, A. Stepanov, J. P. Wolf and V. Sundström, *J. Am. Chem. Soc.*, 2014, **136**, 5189.
8 F. Deschler, M. Price, S. Pathak, L. E. Klintberg, D. D. Jarausch, R. Higler, S. Hüttner, T. Leijtens, S. D. Stranks, H. J. Snaith, M. Atatüre, R. T. Phillips and R. H. Friend, *J. Phys. Chem. Lett.*, 2014, **5**, 1421.
9 A. Kojima, K. Teshima, Y. Shirai and T. Miyasaka, *J. Am. Chem. Soc.*, 2009, **131**, 6050–6051.
10 J. H. Im, C. R. Lee, J. W. Lee, S. W. Park and N. G. Park, *Nanoscale*, 2011, **3**, 4088–4093.
11 I. Chung, B. Lee, J. He, R. P. H. Chang and M. G. Kanatzidis, *Nature*, 2012, **485**, 486–498.
12 B. E. Hardin, H. J. Snaith and M. D. McGehee, *Nat. Photonics*, 2012, **6**, 162–169.
13 W. S. Yang, J. H. Noh, N. J. Jeon, Y. C. Kim, S. Ryu, J. Seo and S. I. Seok, *Science*, 2015, **348**, 1234–1237.
14 http://www.nrel.gov/ncpv/images/efficiency_chart.jpg.
15 M. A. Green, K. Emery, Y. Hishikawa, W. Warta and E. D. Dunlop, *Prog. Photovoltaics*, 2015, **23**, 1–9.
16 S. Sigdel, A. Dubey, H. Elbohy, A. Aboagye, D. Galipeau, L. Zhang, H. Fong and Q. Qiao, *J. Mater. Chem. A*, 2014, **2**, 11448–11453.
17 Y. Rong, Z. Tang, Y. Zhao, X. Zhong, S. Venkatesan, H. Graham, M. Patton, Y. Jing, A. M. Guloy and Y. Yao, *Nanoscale*, 2015, **7**, 10595–10599.
18 J. A. Christians, P. A. Miranda Herrera and P. V. Kamat, *J. Am. Chem. Soc.*, 2015, **137**, 1530–1538.
19 I. Chung, B. Lee, J. He, R. P. H. Chang and M. G. Kanatzidis, *Nature*, 2012, **485**, 486.
20 Z. Xiao, C. Bi, Y. Shao, Q. Dong, Q. Wang, C. Wang, Y. Gao and J. Huang, *Energy Environ. Sci.*, 2014, **7**, 2619.
21 A. Kojima, K. Teshima, Y. Shirai and T. Miyasaka, *J. Am. Chem. Soc.*, 2009, **131**, 6050.
22 J. M. Ball, M. M. Lee, A. Hey and H. J. Snaith, *Energy Environ. Sci.*, 2013, **6**, 1739.
23 D. Liu and T. L. Kelly, *Nat. Photonics*, 2014, **8**, 133.
24 Q. Wang, Q. Dong, Z. Xiao, Y. Yuan and J. Huang, *Energy Environ. Sci.*, 2014, **7**, 2359.
25 N. J. Jeon, J. H. Noh, Y. C. Kim, W. S. Yang, S. Ryu and S. I. Seok, *Nat. Mater.*, 2014, **13**, 89.
26 M. Xiao, F. Huang, W. Huang, Y. Dkhissi, Y. Zhu, J. Etheridge, A. Gray-Weale, U. Bach, Y. B. Cheng and L. Spiccia, *Angew. Chem.*, 2014, **126**, 10056.
27 F. Zhang, J. Lian, J. Song, Y. Hao, P. Zeng and H. Niu, *J. Mater. Chem. A*, 2016, **4**, 3438–3445.

28 Z. Xiao, Q. Dong, C. Bi, Y. Shao, Y. Yuan and J. Huang, *Adv. Mater.*, 2014, **26**, 6503–6509.
29 J. Liu, C. Gao, X. He, Q. Ye, L. Ouyang, D. Zhuang, C. Liao, J. Mei and W. Lao, *ACS Appl. Mater. Interfaces*, 2015, **7**, 24008–24015.
30 K. Yan, M. Long, T. Zhang, Z. Wei, H. Chen, S. Yang and J. Xu, *J. Am. Chem. Soc.*, 2015, **137**, 4460.
31 M. Qian, M. Li, X. B. Shi, H. Ma, Z. K. Wang and L. S. Liao, *J. Mater. Chem. A*, 2015, **3**, 13533–13539.
32 J. You, Y. M. Yang, G. Li and Y. Yang, *Appl. Phys. Lett.*, 2014, **105**, 183902.
33 H. Zhou, Q. Chen, Y. Liu and Y. Yang, *Science*, 2014, **345**, 542–546.